Deposited on 19 February 2024

Characterisation of magnetisation ripple using Lorentz microscopy: Effect of ultra-thin $Ni_{79}Fe_{21}$ seed layers on magnetic properties of $Ni_{45}Fe_{55}$

Alison Cowan[a,], Kevin McNeill[c], Muhammad Bilal Janjua[c], Stephen McVitie[b]

[a]*Natural Magnetism Group, Department of Earth Science and Engineering, Imperial College London, London, SW7 2AZ, UK*
[b]*SUPA, School of Physics and Astronomy, University of Glasgow, Glasgow,G12 8QQ, UK*
[c]*Seagate Technology, Springtown Industrial Estate, Londonderry, BT48 0LY, UK*

Abstract

$Ni_{45}Fe_{55}$ has long been a high moment alternative for $Ni_{80}Fe_{20}$, which is commonly used in hard disk drive (HDD) read-write head design. In this paper we investigate the effect of ultra thin $Ni_{79}Fe_{21}$ seed layers on controlling the physical and magnetic behaviour of $Ni_{45}Fe_{55}$. Transmission electron microscopy (TEM) was used to observe grain size variation. Introducing a seed layer of 0.5 nm thickness reduced the average grain size diameter by over 80% to 2 nm. Diffraction analysis shows texture exists along the [010] direction for the unseeded and 0.25 nm seed layer films. The addition of the $Ni_{79}Fe_{21}$ seed layer reduces film texture. Bulk magnetic measurements showed seed layers improved uniaxial anisotropy, with decreasing easy axis coercivity H_C, and an increase in the anisotropy field H_K. The Fresnel mode of Lorentz microscopy was used to image micromagnetic behaviour during in-situ magnetising experiments. The nano-scale visualisation of the magnetic structure allows for not only the mapping of hysteresis behaviour, but quantitative characterisation of the material in the form of magnetisation ripple. This was characterised in two ways; the ripple dispersion and wavelength. The addition of $Ni_{79}Fe_{21}$ seed layers acted to significantly reduce ripple wavelength and dispersion angle. The dramatic effect of seed layer addition suggests that the ultra-thin film is a good candidate for controlling both the physical and magnetic properties of $Ni_{45}Fe_{55}$ films, whilst maintaining a high magnetic moment density.

Keywords: Soft magnetic materials, polycrystalline, Lorentz microscopy, magnetisation ripple, anisotropy, hysteresis.

1. Introduction

In order to keep pace with the digital storage demands, it is necessary that the capacity of storage devices increases while reducing cost per GigaByte and meeting device reliability requirements [1]. Hard Disk Drives (HDDs) remain an integral and necessary part of the digital storage landscape with continuing demand for increased storage density capability. In order to maintain this, reductions in individual bit sizes are necessary to improve the

systems areal density capability (ADC) [2, 3]. Read-write head development to support these system requirements benefits from high moment, permeable ferromagnetic materials in both the write element and read sensor components of the head for increased write field and improved shielding characteristics respectively [4].

In HDD read-write head design $Ni_{45}Fe_{55}$ has long been a high moment alternative for $Ni_{80}Fe_{20}$, however lack of a well-defined uniaxial anisotropy and higher coercive fields have limited its widespread adoption [5, 6]. $Ni_{45}Fe_{55}$ has an increased magnetic flux density saturation B_S of 1.6 T, compared to 1 T for $Ni_{80}Fe_{20}$. A higher B_S value results in higher write fields, and is an important factor for switching higher coercivity media. It also increases permeability in shielding structures, which provide better protection from unwanted stray fields during read back processes. $Ni_{45}Fe_{55}$ also exhibits a reasonable coercivity (slightly more than $Ni_{80}Fe_{20}$ but lower than higher percentage composition Fe alloys). $Ni_{1-x}Fe_x$ alloys with larger Fe concentration (x>55%) are subject to corrosion in head manufacture and operation in the drive, so are not a viable option. The disadvantages of $Ni_{45}Fe_{55}$ include a $\approx$ 20 fold increase in magnetostrictive effects. HDD devices aim for little to no magnetostriction present in the read/write head materials, however the overall effects of this increase are expected to be negligible [7].

Use of extremely thin seed layers, and ferromagnetic seed layers in particular, are of interest to control the microstructure in such films to achieve soft magnetic properties while maintaining a high magnetic moment density. As read-write head critical dimensions decrease, it is more important than ever to pay particular attention to local, nano-scale magnetic effects as new materials are developed and optimised. A polycrystalline magnetic material will exhibit a phenomenon called magnetisation ripple. It can be defined as the local fluctuation of the magnetization [8]. Fig.1 shows the physical origin of the magnetisation fluctuations which stems from the films < 10 nm granular structure. Fig.1(a) shows a conventional TEM image of the polycrystalline structure whilst Fig.1(b) is a schematic which illustrates the local crystalline anisotropy direction in each grain, which is random, relative to the global induced anisotropy of the film, where the uniaxial anisotropy axis represents the easy directions of magnetisation. Each grain has its own individual crystalline anisotropy K_g, which is often randomly orientated. This local variation of anisotropy results in a deviation of the magnetisation with fluctuations over a few 100 nms, as demonstrated in Fig.1(c). In effect, it produces low-angle domain walls within the film. The magnetisation ripple properties can give an additional insight in the specimens micromagnetic configuration. TEM is proposed as a viable additional micro-structural characterisation. In this paper we explore the physical and micromagnetic properties of $Ni_{45}Fe_{55}$ thin films with increasing seed layer thickness. Imaging with transmission electron microscopy allows the grain size and magnetisation reversal behaviours to be studied in great detail, with specific focus on characterisation of magnetisation ripple.
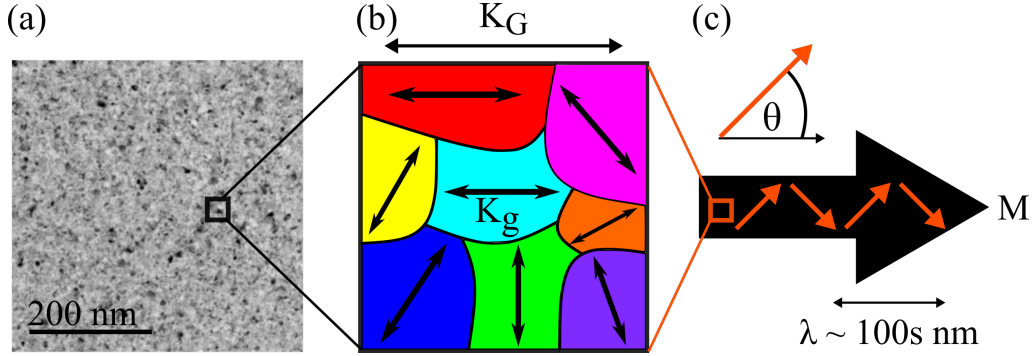
Figure 1: Schematic of magnetisation ripple origin. (a) $Ni_{45}Fe_{55}$ bright field TEM image, showing a granular structure, expected from a polycrystalline thin film. (b) The random direction of the granular crystalline anisotropy K_g, with an additional global uniaxial anisotropy K_G. (c) Schematic of the magnetisation fluctuations, producing low-angle domain walls, commonly referred to as magnetisation ripple, where the length scale is in the order of 100s nm.

2. Experimental Details

Four polycrystalline film stacks with thickness close to 15 nm, were investigated. All films included a 10 nm $Ni_{45}Fe_{55}$ layer, followed by a 5 nm Ru capping layer to prevent subsequent oxidation. Fig.2 shows a schematic illustration of the film structure. In addition to an unseeded sample, samples with seedlayers of 0.25, 0.5 and 1.0 nm $Ni_{79}Fe_{21}$ were investigated. All layers were grown through radio frequency (rf) magnetron sputter deposition using an Anelva c-7100 tool situated at Seagate Technology. A static 100 Oe aligning field was applied in the plane of the film to help induce an uniaxial anisotropy. Deposited films were then annealed in a 0.3 T applied field at 225 degree Celsius (along the same direction as the deposition field). Deposition rates were calibrated by a X-ray fluorescence (XRF) measurement and thickness confirmed with scanning electron microscopy (SEM) measurement of sample cross sections prepared by focused ion beam (FIB). The films were deposited onto $100 \times 100 \ \mu m^2$ electron transparent Si_3N_4 membranes for TEM measurements, as well as bulk Si substrates. Easy and hard axis hysteresis loops for each film were determined using a SHB model 109A hysteresis loop tracer, operating at a maximum applied field of 200 Oe.

TEM specimens were examined with a FEI Tecnai T20 instrument operated at 200 keV. Bright-field (BF), dark-field (DF) images were acquired to measure the distribution of grain sizes. Diffraction patterns were acquired to determine the specimens crystal structure and film texture, taken at various orientations with respect to the electron beam.

The magnetic structure and reversal mechanisms were characterised using the same microscope. For Lorentz microscopy studies, standard TEM microscopes are modified through the addition of Lorentz lenses below the objective lens. This creates a low field environment for the specimen as the objective lens can be switched off, and the lower Lorentz lens acts as the imaging lens. Magnetising experiments were carried out by weakly exciting the objective lens to produce a magnetic field perpendicular to the plane of the specimen. Tilting the specimen introduces a component of the field in the plane of the specimen, therefore allowing for direct, *in-situ* magnetising observations and experiments. A maximum applied field of $\pm$
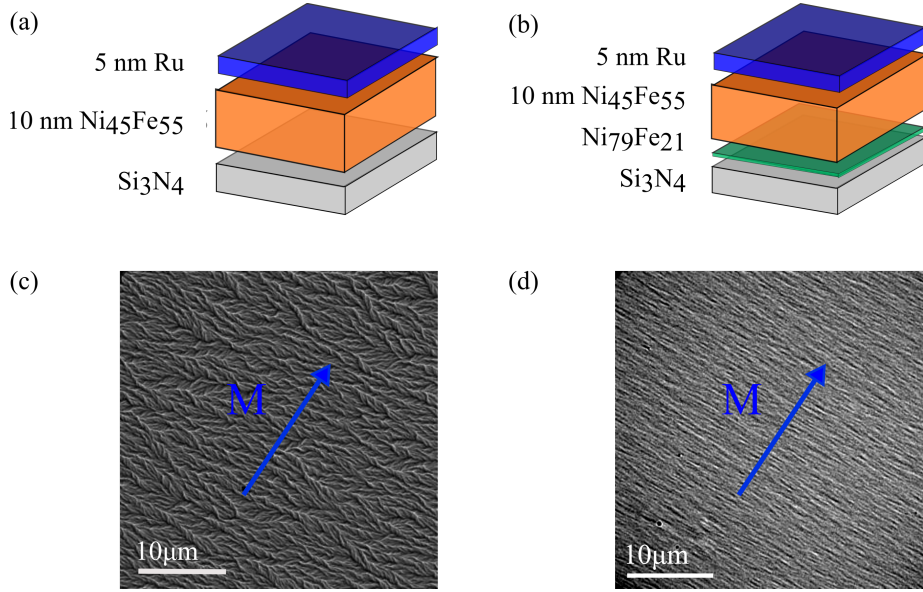
3

Figure 2: Cross section schematic showing the structures of samples (a) unseeded, (b) seeded samples with the following seed layer thickness; 0.25 nm $Ni_{79}Fe_{21}$, 0.5 nm $Ni_{79}Fe_{21}$ and 1.0 nm $Ni_{79}Fe_{21}$. All samples consist of a 10 nm $Ni_{45}Fe_{55}$ layer, and are capped with a 5 nm Ru layer. All samples were deposited on electron transparent Si_3N_4 membranes. (c,d) Corresponding experimental Fresnel images for unseeded and 1 nm seeded sample respectively highlighting ripple variation.

24 Oe could be achieved through a tilt angle of $\pm$ 30 degrees (corresponding to a remanent field of 60 Oe being present in the microscope column). An out-of-plane component is also present, but has a negligible effect as the demagnetising factor for a thin film means that the magnetisation will remain in plane in the presence of the weak out of plane field. Therefore, only the in-plane component needs to be considered for the following work.

The main imaging mode used for acquiring the magnetic configuration of the material is the Fresnel mode of Lorentz microscopy [9, 10, 11, 12]. This is a defocused method where contrast arises due to the classical Lorentz interaction arising from the component of magnetic induction perpendicular to the electron beam which results in a deflection of the beam. A Fresnel image normally shows domain walls as lines of black and white contrast. In the case of magnetisation ripple the configuration is like closely spaced low angle domain walls. As discussed previously in the introduction, magnetisation ripple is the small wave-like fluctuations of the magnetisation direction, which originates from the random orientation of the local anisotropies in each grain. The magnetisation ripple contrast lies perpendicular to the mean direction of the local magnetisation as shown in Fig.2(c,d). It can be used to orient the specimen with the applied field along either the easy or hard axis.

3. Results and Discussion

3.1. Bulk Magnetic Measurements

Fig.3 shows the normalised easy and hard axis hysteresis loops from the B-H loop measurements on the four films. The red and blue loops represent the applied field along the easy

4

and hard directions respectively. Note that easy axis direction is defined from the field axis used during deposition and annealing. The unseeded film, shows near isotropic behaviour with a large coercivity of 29 Oe along the defined easy axis, and little change when applied along the hard direction. Therefore, the fields used during deposition and annealing have not resulted in anisotropic behaviour.

With the introduction of a thin 0.25 nm $Ni_{79}Fe_{21}$ seed layer some anisotropic behaviour can be seen, evidenced through a decreasing easy axis coercivity. There is also a marked increase in anisotropic behaviour, as evidenced by the increase in H_K. The anisotropy becomes much better defined with the addition of thicker seed layers. Improved anisotropic behaviour increases significantly for 0.5 nm with the 1.0 nm showing almost identical behaviour.
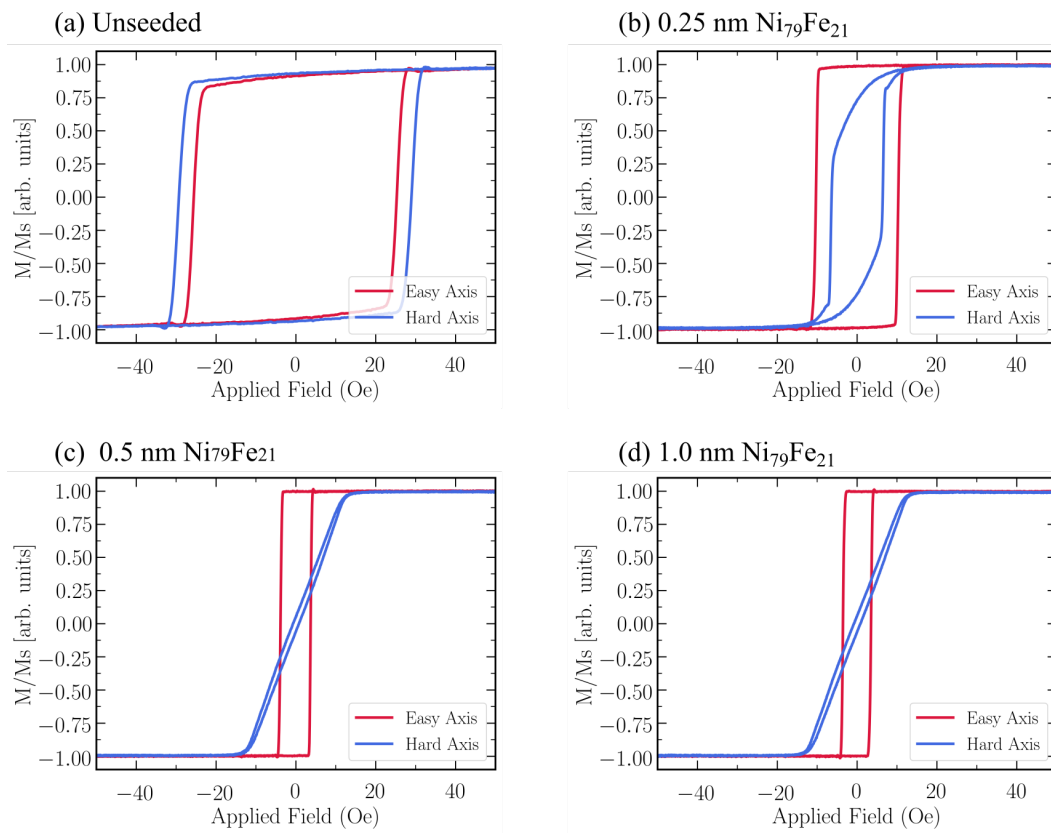
Figure 3: Hysteresis loops for 10 nm NiFe55 sample (a) unseeded, (b) 0.25 nm $Ni_{79}Fe_{21}$ seed layer, (c) 0.5 nm $Ni_{79}Fe_{21}$ seed layer and (d) 1.0 nm $Ni_{79}Fe_{21}$ seed layer, with the field applied along the easy and hard axis, represented by the red and blue loops respectively.

It appears that the increasing seed layer results in excellent definition of uniaxial anisotropy which looks to have not further improved at 1 nm seed layer thickness. Therefore in terms of anisotropy definition a seed layer thickness between 0.5 and 1.0 nm is suitable for good anisotropic behaviour for this system. The addition of increasing thickness seed layer increased the magnetic moment of the film. Magnetic flux density values increased from 1.42 to 1.57 T for the unseeded to 1.0 nm seeded sample. There is quite clearly a significant

improvement in magnetic properties, such as the reduction in H_C and an increase in H_K through the addition of $Ni_{79}Fe_{21}$ seed layers when investigating bulk magnetic properties.

3.2. Grain Size Distribution

Before looking at the micromagnetic behaviour of the films we firstly present an investigation of the physical structure of the films. Bright-field and dark-field TEM images were used to analyse the grain size distribution of the film, where the objective aperture was placed on the brightest diffraction ring, *100 hcp*. Fig.4(a-d) visually demonstrates the reduction in grain size with the addition of increasing $Ni_{79}Fe_{21}$ seed layer thickness using dark-field imaging. A seed layer as thin as 0.25 nm (Fig.4(b)) has a noticeable effect on the samples average grain size. Not only do the grains appear to decrease in size, but the spread of the sizes observed is greatly reduced. A seed layer of 0.5 and 1.0 nm (Fig.4(c,d)) significantly reduces the average grain size further. Dark field images are useful when investigating grain size distributions due to the high contrast between the grains. This makes it easier to distinguish individual grains for analysis. The growth processes in granular systems are known to follow a log-normal distribution where the probability distribution *P(D)* of the grains is defined as [13]:

$$P(D) = \frac{1}{\sqrt{2\pi}\sigma D} exp\left[\frac{-(ln(D) - \mu)^2}{2(\sigma)^2}\right] \tag{1}$$

where D is the grain diameter, μ is the mean value of *ln(D)* and σ is the standard deviation of *ln(D)*.

To measure the grain size, a large number of dark-field images were acquired to ensure statistical significance (> 20 images). Image processing can be carried out using the software Image J, where limits of minimum and maximum grey levels can be selected to produce a threshold image, and the individual grain sizes measured. The best-fit log-normal distribution can then be plotted against the measured diameters, as shown in Fig.4(e). To ensure good statistical results, a minimum of 10,000 grain diameters were measured for each specimen.

Not only do the grains appear to decrease in size (Table 1), the spread of sizes also reduces. The measured log-normal (mode) peak decreases from a grain size diameter of 10 nm in the unseeded film, to 7 nm in the 0.25 nm seed layer sample, then proceeds to saturate at just under 2 nm for 0.5 nm seed layer. The narrow distribution of grains confirms homogeneity of nano-grains existing in the 0.5 and 1.0 nm films. It is suggested that by reducing the grain size below the exchange length ($L_{ex} = \sqrt{A/\mu_0 M_s^2}$), typically 5-10 nm, it will lead to more efficient in-plane exchange coupling between the individual grains. An effect of a stronger granular exchange coupling might be expected to suppress the magnetisation ripple in the film.

3.3. Crystal Structure

NiFe alloys used in the seeded layer, with a composition of 79/21 have a *fcc* structure. The 10 nm NiFe alloy with a composition of 45/55 has a *bcc* crystal structure. The Ru

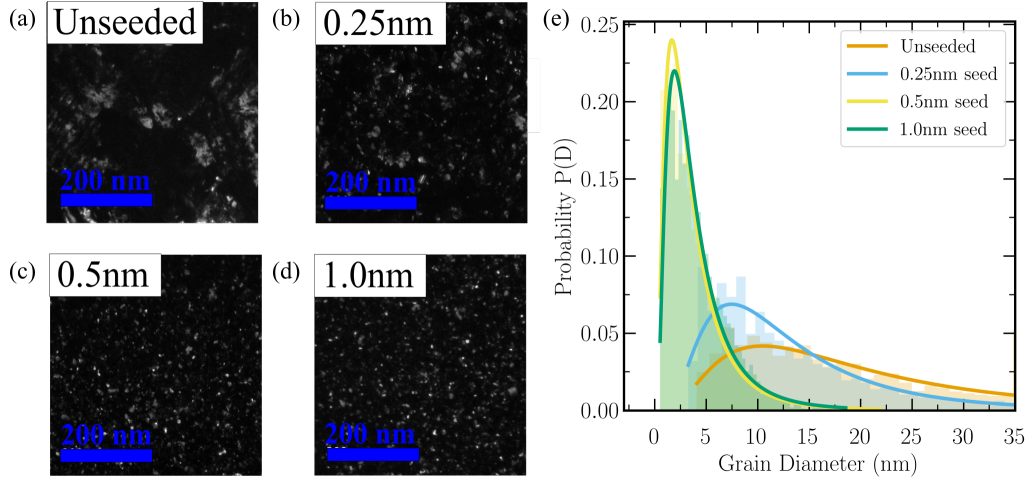Figure 4: Experimental dark-field TEM images, displaying the grain size distribution for a 10 nm $Ni_{45}Fe_{55}$ sample (a) unseeded, (b) 0.25 nm $Ni_{79}Fe_{21}$, (c) 0.5 nm $Ni_{79}Fe_{21}$ and (d) 1.0 nm $Ni_{79}Fe_{21}$ seed layer. The best-fit log-normal distribution can be determined from experimental measurements using Equation (1) and is displayed in (e).

Seedlayer Thickness (nm)	Mean Diameter (nm)	Log-normal Peak (nm)
0.00	17	10
0.25	11	7
0.50	3	2
1.00	3	2

Table 1: Grain size distribution analysis outputs.

layer is a *hcp* structure. These crystal structures are known for these compositions. Experimental diffraction images allow for these structures to be confirmed with selected area electron diffraction (SAED) measurements. Diffraction allows for the identification of crystal structures and lattice parameter measurements. However, care is needed in analysing and indexing electron diffraction patterns when imaging multi-layer stacks. Fig.5 shows SAED images for films that are (a) unseeded and untilted, followed by samples tilted by 20 degrees for: (b) unseeded, (c) 0.25 nm $Ni_{79}Fe_{21}$ seeded, and (d) 1.0 nm seeded sample.

The uniform circular diffraction rings surrounding a single central spot obtained from an untilted sample confirms that the sample is polycrystalline. The combination of several crystal structures results in the rings within the seeded samples shown in Fig.5(c,d) overlapping, creating rings with larger widths.

It is well know that when tilting a non-textured polycrystalline specimen, the diffraction pattern rings maintain their uniform intensity radially. However, in the case of a textured polycrystalline film, the pattern will have broken rings, or arcs i.e. the intensity of some rings is either enhanced or reduced. This indicates that the grains in the film are not randomly oriented but in fact display a preferred orientation. The SAED images shown in Fig.5 show

Figure 5: SAED patterns for an unseeded and (a) untilted sample, and (b) a 20 degree tilt angle. Frames (c) and (d) show the SAED patterns for the (c) 0.25 nm seeded sample, and (d) shows the 1.0 nm seeded sample, both at a tilt angle of 20 degrees.

that there is texture present in the unseeded and 0.25 nm seed layer sample. Analysis shows texture exists along the [010] direction for the unseeded and 0.25 nm seed layer films. The addition of the $Ni_{79}Fe_{21}$ seed layer reduces the texture in the thin film, demonstrated by the unbroken diffraction rings present in the 1.0 nm seed layer sample. Seed layers are often used to promote a crystal texture direction, whereas the opposite effect is seen here [5, 14]. However, as the seed layers used in this investigation are ultra-thin (≤ 1 nm), it is proposed that they in-fact don't act like conventional seed layers, but provide nucleation sites for the growing film, leading to a reduced average grain size and more randomised texture directionality [15].

3.4. Magnetisation Reversal

In-situ visualisation of the magnetic configuration by TEM imaging allows for mapping of easy and hard axis hysteresis behaviour, but on the micromagnetic scale. This provides further insight into variations in reversal processes. Magnetisation ripple allows the orientation of the magnetisation to be determined as it lies perpendicular to the dominant longitudinal ripple [16].

For an applied field lying parallel to the easy axis of the magnetic thin film, magnetisation reversal normally proceeds by a single 180° domain wall sweeping across the sample [17, 18]. As can best seen for the films with well defined uniaxial anisotropy the loops are quite square (Fig.3(c,d)), therefore at reversal any walls sweep rapidly at this field. During imaging this

was apparent as a rapid change but with no domain wall visible. The externally applied field was increased slowly in the opposite direction to the mean magnetisation direction to get in close approximation to the coercive field H_C of the sample.

Experimental Fresnel images were acquired of the easy and hard axis magnetisation reversal for the unseeded and all seeded samples. Easy axis behaviour is expected to include a sudden switch of magnetisation direction at the coercive field. Idealised hard axis behaviour includes a rotation of the magnetisation direction for an uniaxial film.

Fig.6(a-e) shows example images of the typical reversal mechanism along the easy axis of the 0.5 nm seed layer sample displaying strong uniaxial anisotropy. There was a small visible increase of the magnetisation ripple dispersion when reducing the field from the magnetisation saturation state, seen in (a)-(c). There is a sudden change of magnetisation direction, where **M** and **H** go from anti-parallel to parallel in (c) to (d), in which the domain wall sweep occurs too quickly to be imaged. This was followed by a suppression of the ripple after the coercive field was achieved. (d)-(e).
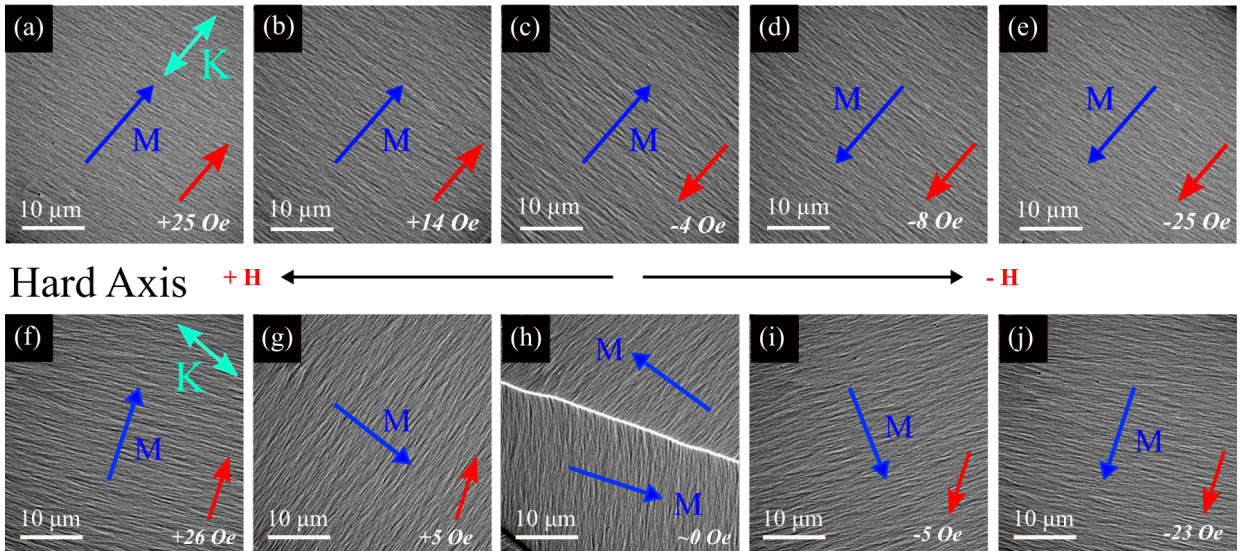
Easy Axis

Hard Axis

Figure 6: Experimental Fresnel images demonstrating the magnetisation reversal process along the easy axis (a-e) and hard axis (f-j) of 10 nm $Ni_{45}Fe_{55}$ thin film with 0.5 nm $Ni_{79}Fe_{21}$ seed layer. The red arrows represent the direction of the applied field, H, and K is the uniaxial anisotropy direction. (a-e) There is a visible increase in magnetisation ripple contrast until the coercive field H_C is reached (d-e), and the direction of magnetisation rapidly switches. (f-j) Typical hard axis behaviour with a rotation of the magnetisation direction by 90 degrees with a reduced applied field followed by domain formation at zero field (h).

Typical hard axis hysteresis behaviour was observed and is shown in Fig.6(f-j). The applied field is reduced from (f-h). The magnetisation direction begins to rotate, before domain walls begin to appear in (h). The magnetisation of the domains lies parallel to the easy axis direction, which is typical hard axis behaviour for a thin film with a strong uniaxial anisotropy present. The domain increased in size with increasing field (in the opposing direction), gradually covering the whole area of the membrane, through the movement of

the domain wall. A larger applied field forces the magnetisation direction from the easy axis direction, to the perpendicular hard axis. Reversal images were acquired for all sets of samples. The variation in their configurations and quantitative analysis will be discussed in the following section.

Figure 7 highlights key points of the hysteresis sequence for different unseeded and seeded samples for both easy and hard axis behaviours at +24 Oe (almost saturated) and at 0 Oe (remanence) respectively. The easy axis B-H loop (Fig.7(a)) denotes that all the 3 samples have nearly the same M/Ms value at the field of +24 Oe, measuring at 0.93, 0.99 and 0.99 respectively. However, the observed ripple behaviour in the seed layer samples depends strongly on the seed layer thickness. The unseeded sample (Fig.7(b,f)) visually exhibited a large amount of ripple dispersion, and much more irregular structure when compared to the seeded films. It was observed that there was little to no difference between the 'easy' and 'hard' axis loops, confirming the bulk measurements which showed a lack of defined anisotropy axis. The 0.25 nm seeded sample (Fig.7(c,g)) showed improved uniaxial anisotropy evidenced through a reduction of ripple dispersion and image contrast, when compared to the unseeded sample. However it still retained some magnetisation at remanence, highlighted by the irregular domain formation in Fig.7(g). The 0.5 nm seeded sample (Fig.7(d,h)) exhibited typical easy and hard axis reversal processes, with a strong uniaxial anisotropy. Again, there is a substantial visual suppression in the angular dispersion of the ripple when compared to the 0.25 nm seeded sample. Similar hysteresis processes and ripple configurations were observed for 0.5 nm and 1.0 nm seed layer films. Whilst it is evident that the introduction of the seed layers has resulted better uniaxial behaviour and certainly a clear visual difference in ripple, we now use the TEM data to quantify the latter.

3.5. Magnetisation Ripple Characterisation

Quantitative outputs of magnetisation ripple properties gives additional insight into the micromagnetic processes of the samples described, which are not seen from bulk measurement techniques [19, 20]. Here we propose two different FFT methods to characterise magnetic ripple: (1) ripple dispersion i.e. the angle of deviation from the mean magnetisation direction and (2) ripple wavelength [21]. We illustrate the methodology on a typical experimental Fresnel image in Fig.8(a). The image allows determination of the axis along which the magnetisation is located, however it should be noted that the direction of magnetisation is deduced from the field history.

A fast Fourier transform (FFT) shows the spatial frequency spectrum of an image allowing the ripple components and character to be identified and quantified. The FFT produces a 'bow-tie' structure in Fourier space as shown in Fig.8(b). The bow-tie structure consists of two lobe-like features. There is a 2-fold symmetry associated with the structure, so only half of the bow-tie structure will be considered.

Intensity profiles are taken from the centre of the FFT to the edge of the image for a range of π. Each line profile is integrated to get the total intensity. This value is plotted for all angles as shown in (c). The width of this peak can give information on the spread of the magnetic ripple orientation, and is referred to as the magnetic ripple dispersion, θ. The desired quantitative output is the full-width half maximum (FWHM) of the peak. A
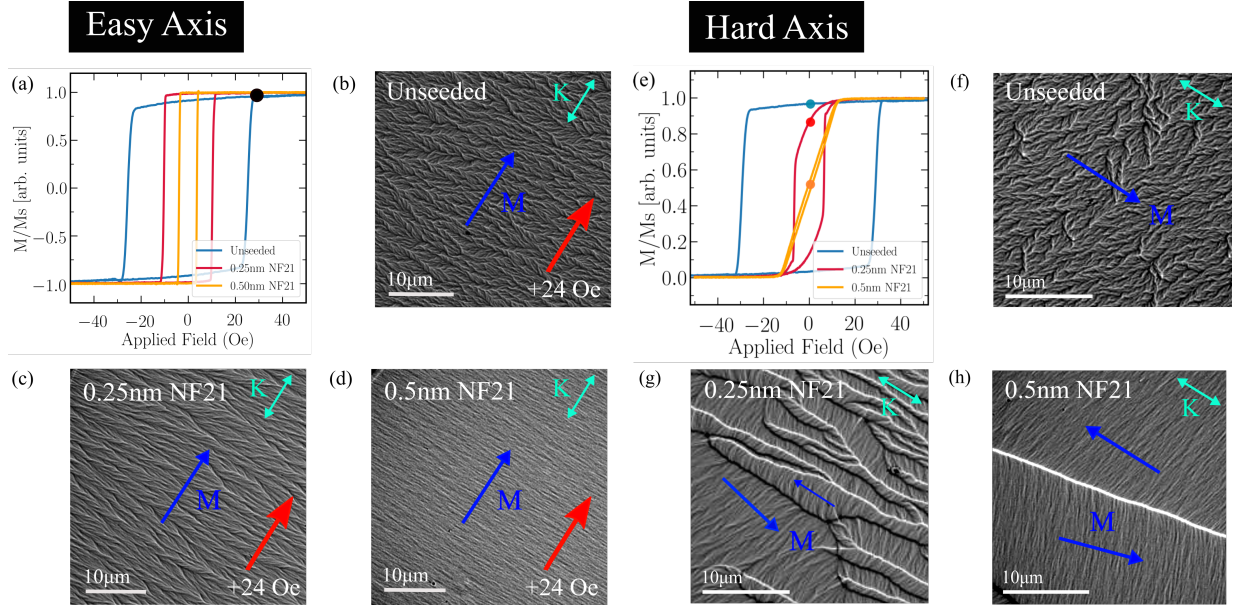
Figure 7: (a,e) B-H hysteresis plot for unseeded, 0.25 nm, 0.5 nm $Ni_{79}Fe_{21}$ seed layer, 10 nm $Ni_{45}Fe_{55}$ thin films with the field applied along the easy and hard axis respectively. Easy axis experimental Fresnel TEM images showing the suppression of magnetisation ripple are shown in (b,c,d). All images were acquired with an externally applied field of +24 Oe, shown by the black dot on the hysteresis plot. Visually displays the suppression of magnetisation ripple through the addition of ultra thin $Ni_{79}Fe_{21}$ seed layers. Hard axis magnetic configuration at remanence are shown in (f,g,h) highlighting the variation in domain formation (g,h), if any (f). Different scales should be noted.

best-fit Lorentzian curve can be applied to the data. A large increase in the dispersion angle is normally seen in easy axis reversal processes, when an applied field is reduced from magnetisation saturation to just before the switching field, H_C is reached.

It can be seen from the experimental Fresnel images that they contain a range of spatial frequency information, this is clear from the FFT. We can use the latter to determine the ripple values associated with the image. The method described here is used to determine the weighted mean of all the ripple wavelength values present in the FFT, and will be referred to as the spectral centroid wavelength value.

Similarly to dispersion angle determination, a FFT is taken of an experimental Fresnel image Fig.8(a) as shown in (b). This bow-tie structure contains a range of wavelength frequencies. A newly developed method to characterise a single ripple wavelength value is to use a partial integration technique on the FFT bow-tie structure. This process includes integrating radially, by a width of a pixel, specifically in the region previously determined by the dispersion angle (c). The intensities that lie along these lines are summed and averaged. These values can be plotted against distance from the origin, i.e. plot the radial averaged integrated intensity against inverse wavelength (measured in reciprocal k-space) and are shown in (d).

The spectral centroid wavelength value is calculated as the weighted mean of the fre-

(a) Experimental Lorentz image

(b) Modulus of FFT of Lorentz image in (a)

(c) Lorentzian fit with FWHM indicated by black dashed line

(d) Measured integrated intensity against k-space. Dashed line represents the wavelength spectral centroid
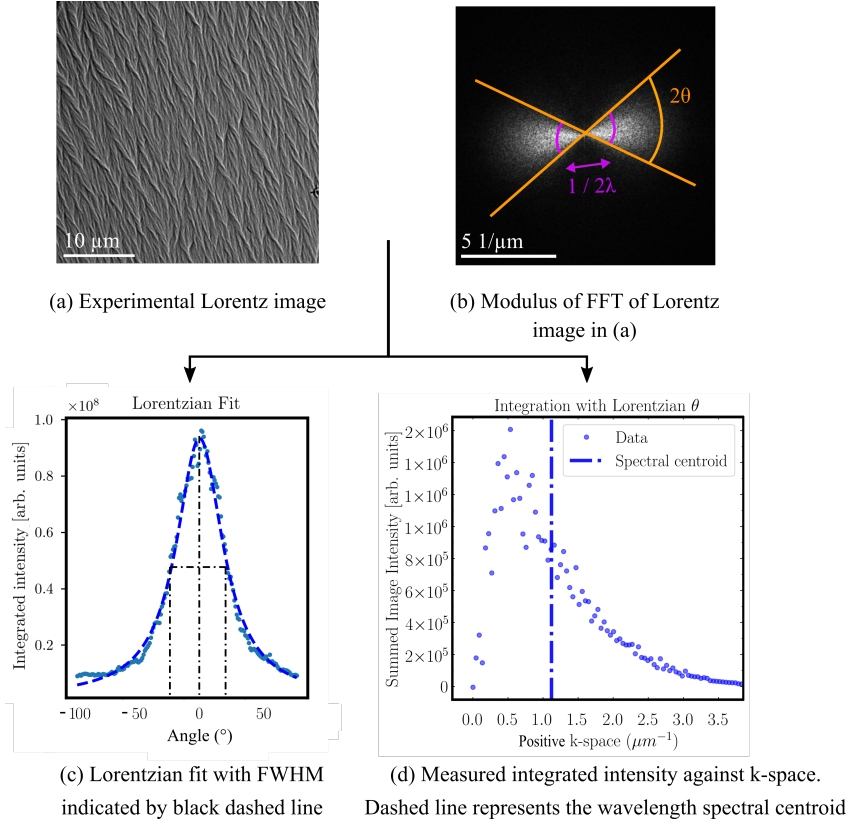
Figure 8: Schematic of magnetisation ripple dispersion and wavelength determination from an experimental Fresnel image (a) and corresponding FFT (b). (c) The integrated intensity value profile can be plotted as a function of angle. A best fit Lorentzian curve is used for accurate determination of the peak FWHM. (d) displays a plot of integrated intensity from the FFT origin against FFT k-space distance. Ripple wavelength is determined the weighted mean of ripple frequencies. This measured value is highlighted by the bold vertical line.

quencies present in the signal. The spectral centroid value for the distribution is measured through relative intensities and their distances in k-space. It can be written as:

$$\lambda_{spectral\ centroid} = \frac{\sum k \cdot I(k)}{\sum I(k)} \tag{2}$$

where $I(k)$ represents the integrated intensity of the bin, and k represents the centre frequency of that bin.

3.5.1. Magnetisation Ripple Characterisation Results

The unseeded and seeded samples were characterised using methods described for full easy and hard axis sequences, to determine the relation between magnetisation ripple properties and seed layer thickness. For simplicity, only key points of the hysteresis sequence will be highlighted and discussed.

Fig.9 shows a direct comparison of Lorentzian fits of integrated intensities for varying seed layer samples along the easy axis; pre-switch at the coercive field H_C (a) and at an

12

applied field of 24 Oe (b) for dispersion angle θ. A field of 24 Oe was chosen as a field where **M** and **H** are parallel and represent a state approaching saturation. In comparison the pre-switch H_C had **M** and **H** lying anti-parallel with significant ripple dispersion.
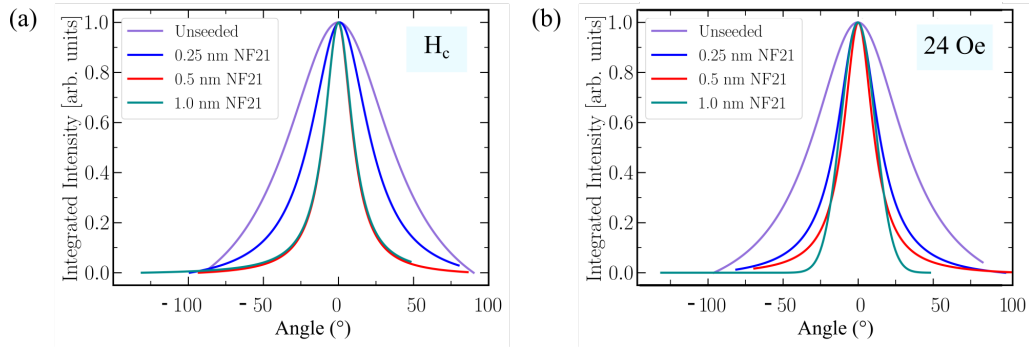

Figure 9: Easy axis FFT analysis comparison for varying thickness of $Ni_{79}Fe_{21}$ seed layers. (a,b) display the suppression of the deviation from the magnetisation **M** direction with increasing seed layer thickness, using the Lorentzian fitting method. (a) is measured at the samples relative coercive field H_C before switching, where as (b) is measured at a field of +24 Oe approaching magnetisation saturation.

All samples exhibited a measurable suppression of ripple dispersion with increasing field (Table 2), confirming what was visually seen from experimental Fresnel images (Fig.6), and by theory predictions [21]. There is a gradual decrease in deviation from the mean magnetisation direction with increasing seed layer thickness. This is consistent for both measurements taken at the coercive field value (a) and an applied field of 24 Oe (b). Measured values are shown in Table 2.

Fig.10 shows the integrated intensity plots and corresponding spectral centroid wavelength measurements (indicated by the vertical dashed line) at the same conditions: (a) pre-switch at the coercive field H_C and (b) at an applied field of 24 Oe. The unseeded sample was not measurable using the described method in Fig.10(d,e). The average wavelength was approximated using the method shown in Fig.8(d). Plots shown in Fig.10(a,b) follow the same trends seen from dispersion angle results. There is a decrease of the weighted average wavelength value with increasing seed layer thickness. Additionally, the ripple wavelength decreases with increasing applied field for all samples. Furthermore, there is a decline in the image integrated intensity (y-axis) with increasing seed layer thickness, which is expected due to the reduced image contrast. Results presented here reiterate that the addition of seed layers improves the films uniaxial anisotropy, which is evidenced through a considerable in both ripple dispersion and wavelength properties.

The quantitative wavelength outputs are highlighted in Table 2. Outputs for H_C, 0 and +24 Oe field were chosen to measure the maximum, remanent, and parallel **M** and **H** configuration, approaching saturation respectively for direct comparison with varying seed layer thickness. The addition of a 1.0 nm seed layer can suppress the ripple wavelength from 1.10 μm to 0.56 μm when measured at the films coercive field (50% decrease). The same trends were seen for the dispersion angle measurements, seeing a reduction from 43° to 11° when comparing the unseeded film to the 0.5 nm and 1.0 nm seed layer films, which were
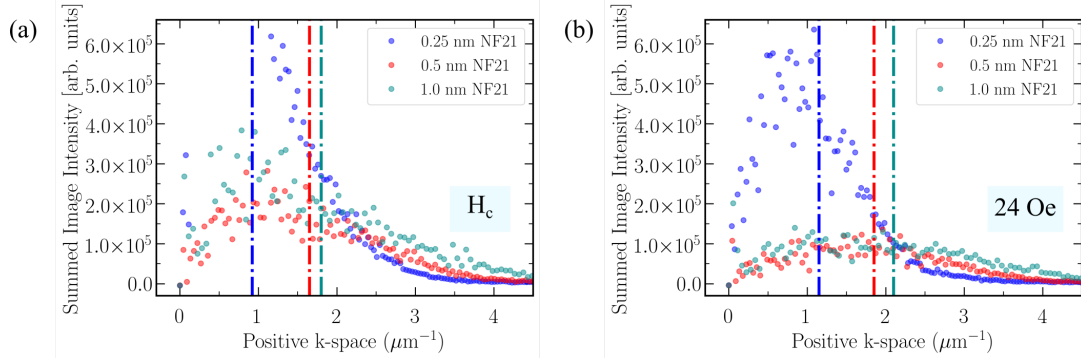
Figure 10: Easy axis magnetisation ripple characterisation outputs for varying thickness of $Ni_{79}Fe_{21}$ seed layers. Determined spectral centroid wavelength value indicated by the vertical dashed line. (a) is measured at the samples H_C before the switch in $\mathbf{M}$ direction, where as (b) is measured at a field of $+24$ Oe approaching M_{Sat}. (a,b) show the shift of the spectral centroid in k-space with increasing field. There is also a note-able decrease in the images integrated intensity peak with increasing seed layer thickness.

themselves very similar.

Seed layer Thickness (nm)	Dispersion Angle θ (°)			Wavelength λ (μm)		
	H_C (Oe)	0 Oe	24 Oe	H_C (Oe)	0 Oe	24 Oe
0.00	43	42	37	1.10	1.10	1.08
0.25	23	19	16	1.08	1.00	0.88
0.50	11	11	11	0.62	0.60	0.54
1.00	11	11	11	0.56	0.54	0.48

Table 2: Key outputs from ripple analysis. The ripple dispersion angle and spectral centroid wavelength was investigated as a function of field, applied along the easy axis. Table includes outputs for each seed layer sample at an applied field of 24 Oe, remanence, and at the corresponding coercive field H_C before the switch in magnetisation direction.

Analysis techniques display the same conclusions: there is a large suppression of ripple properties when increasing seed layer thickness from 0.25 nm to 0.5 nm, and this effect seems to plateau with the addition of a thicker seed layer, in this case 1.0 nm.

4. Summary and Conclusions

This paper shows the influence of ultra-thin $Ni_{79}Fe_{21}$ seed layers on the physical and magnetic microstructure of thin $Ni_{45}Fe_{55}$ films with soft magnetic properties. An addition of ultra-thin seed layers drastically reduces the average grain size of the film by up to 75% (and below exchange length) when compared to an unseeded film, with an associated reduction in grain size distribution. Additionally the presence of seed layers reduces texture in the film, meaning the films grains are randomly oriented in 3 dimensions. Bulk magnetic measurements showed a dramatic improvement in uniaxial anisotropy with increasing seed

14

layer thickness. The unseeded sample showed near isotropic behaviour, whilst the addition of seed layers produced well-defined uniaxial hysteresis loops, with decreasing easy axis coercivities H_C, and an increase in the anisotropy field H_K. Visualisation of magnetisation ripple through Lorentz microscopy allowed for further insight and characterisation of the micromagnetic properties for the different seeded films. A methodology was proposed for characterisation of two magnetisation ripple properties; the ripple dispersion angle, θ and spectral centroid wavelength, λ. The unseeded sample exhibited very pronounced ripple with large amount of dispersion and a large ripple wavelength. The addition of seed layers results in dispersion angle and ripple wavelength values at 25% of the values seen in the unseeded film. The 0.5 nm and 1.0 nm samples had a very subtle suppression of magnetic properties, suggesting a thicker seed layer sample would not improve magnetic properties further. The dramatic effect of seed layer addition suggests that the film is a good candidate for controlling both the physical and magnetic properties of $Ni_{45}Fe_{55}$ thin films, whilst maintaining a high magnetic moment density.

5. Acknowledgements

Appendix A. Section in Appendix

References

[1] D. Weller, G. Parker, O. Mosendz, E. Champion, B. Stipe, X. Wang, T. Klemmer, G. Ju, A. Ajan, A HAMR media technology roadmap to an areal density of 4 Tb/in2, IEEE Transactions on Magnetics 50 (1) (2014).

[2] R. Wood, Future hard disk drive systems, Journal of Magnetism and Magnetic Materials 321 (2009) 555–561.

[3] Y. T. Chen, J. Y. Tseng, T. S. Sheu, Y. C. Lin, S. H. Lin, Effect of grain size on magnetic properties and microstructure of Ni 80Fe20 thin films, in: Thin Solid Films, 2013.

[4] G. Scheunert, O. Heinonen, R. Hardeman, A. Lapicki, M. Gubbins, R. M. Bowman, A review of high magnetic moment thin films for microscale and nanotechnology applications, Applied Physics Reviews 3 (1) (2016).

[5] B. Warot, J. Imrie, A. K. Petford-Long, J. H. Nickel, T. C. Anthony, Influence of seed layers on the microstructure of NiFe layers, in: Journal of Magnetism and Magnetic Materials, 2004, pp. 272–276.

[6] N. Robertson, H. L. Hu, Ching Tsang, High performance write head using nife 45/55, IEEE Transactions on Magnetics 33 (5) (1997) 2818–2820.

[7] C. B. Hill, W. R. Hendren, R. M. Bowman, P. K. Mcgeehin, M. A. Gubbins, V. A. Venugopal, Whole wafer magnetostriction metrology for magnetic films and multilayers, Meas. Sci. Technol. Meas. Sci. Technol 24 (24) (2013) 45601–45601.

[8] H. Hoffmann, Quantitative calculation of the magnetic ripple of uniaxial thin permalloy films, Journal of Applied Physics 35 (6) (1964) 1790–1798.

[9] J. Chapman, High resolution imaging of magnetic structures in the transmission electron microscope, Materials Science and Engineering: B 3 (4) (1989) 355–358.

[10] S. A. Nepijko, G. Schönhense, Quantitative lorentz transmission electron microscopy of structured thin permalloy films, Applied Physics A 96 (3) (2009) 671–677.

[11] J. Tang, Lorentz transmission electron microscopy for magnetic skyrmions imaging, Chinese Physics B 28 (8) (2019).

[12] C. Phatak, Recent advances in Lorentz microscopy, Current Opinion in Solid State and Materials Science 20 (2016) 107–114.

[13] G. Vallejo-Fernandez, Mechanisms of hyperthermia in magnetic nanoparticles, Journal of Physics D: Applied Physics 46 (31) (2013).

[14] D. Litvinov, T. O'Donnell, R. Clarke, In situ thin-film texture determination, Journal of Applied Physics 85 (4) (1999) 2151–2156.

[15] G. Wahyu Alam, E. Pihan, B. Marie, N. Mangelinck-Noël, Impact of the initial growth interface on the grain structure in hpmc-si ingot, in: 2017 IEEE 44th Photovoltaic Specialist Conference (PVSC), 2017, pp. 1498–1503.

[16] D.-T. Ngo, L. T. Kuhn, In situ transmission electron microscopy for magnetic nanostructures, Advances in Natural Sciences: Nanoscience and Nanotechnology 7 (4) (2016) 045001.

[17] S. McVitie, J. N. Chapman, Coherent lorentz imaging of soft, thin-film magnetic materials, MRS Bulletin 20 (10) (1995) 55–58.

[18] A. Gentils, Variation of domain-wall structures and magnetization ripple spectra in permalloy films with controlled uniaxial anisotropy, Journal of Applied Physics 98 (5) (2005) 0–7.

[19] T. Suzuki, C. H. Wilts, Quantitative Study of the Magnetization Ripple in Ferromagnetic Ni–Fe Alloy Films, Journal of Applied Physics 39 (2) (1968) 1151–1153.

[20] J. D. Hosson, Ultrasoft magnetic films investigated with Lorentz transmission electron microscopy and electron holography, Microscopy and Microanalysis 8 (4) (2002) 274–287.

[21] H. Hoffmann, Theory of Magnetization Ripple, 1 4 (1) (1968) 32–38.